# Orbital-selective electron correlations in high- $T_c$ bilayer nickelates: from a global phase diagram to implications for spectroscopy

Zhiguang Liao,<sup>1,\*</sup> Yiming Wang,<sup>2,\*</sup> Lei Chen,<sup>2,3</sup> Guijing Duan,<sup>1</sup> Rong Yu,<sup>1,4,†</sup> and Qimiao Si<sup>2,‡</sup>

<sup>1</sup>Department of Physics and Beijing Key Laboratory of Opto-electronic Functional Materials & Micro-nano Devices,
Renmin University of China, Beijing 100872, China

<sup>2</sup>Department of Physics & Astronomy, Extreme Quantum Materials Alliance,
Smalley Curl Institute, Rice University, Houston, Texas 77005, USA

<sup>3</sup>Department of Physics and Astronomy, Stony Brook University, Stony Brook, NY 11794, USA

<sup>4</sup>Key Laboratory of Quantum State Construction and Manipulation (Ministry of Education),
Renmin University of China, Beijing, 100872, China

Motivated by the high temperature superconductivity observed in the bilayer nickelate  $\text{La}_3\text{Ni}_2\text{O}_7$  and the spectroscopic evidences of strong electron correlations in this compound, we address the role of its multiorbital electron correlations by proposing a global phase diagram of a bilayer two-orbital Hubbard model. We find a Mott transition developing at half filling, and identify strong orbital selectivity when the system is at the physical electron count. The orbital selectivity is manifested in the formation of interlayer spin singlets between electrons in the  $z^2$  orbitals. These features lead to a strong renormalization of the electronic band structure while sustaining a sizable splitting between the bonding and antibonding  $z^2$  bands. The proposed orbital-selective correlations naturally explain a series of features as observed in the angular resolved photoemission spectroscopy (ARPES) and optical conductivity measurements in  $\text{La}_3\text{Ni}_2\text{O}_7$ . Our results provide a basis to understand both the normal state and the high temperature superconductivity of multilayer nickelates and thereby elucidate correlated superconductivity in general.

Introduction. The discovery of superconductivity about 80 K in the bilayer nickelate La<sub>3</sub>Ni<sub>2</sub>O<sub>7</sub> under high pressure [1] is of extensive current interest. Notwithstanding concerns on the structural imperfection [2–4], evidence for the bulk nature of the superconductivity is growing [5, 6], and superconductivity has very recently been seen in thin films at ambient pressure [7]. While their phenomenology, with superconductivity developing upon the suppression of an electronic order, bears some similarities with other families of correlated superconductors, the microscopic electronic physics of the bilayer nickelates has some clear distinction. Unlike the infinitelayer nickelate (Sr,Nd)NiO<sub>2</sub> thin films [8], which parallels the high- $T_c$  cuprates [9] in that it shares the latter's 3d<sup>9</sup> electron configuration from the Ni<sup>+</sup> ion, La<sub>3</sub>Ni<sub>2</sub>O<sub>7</sub> has a valence count of Ni<sup>+2.5</sup>, corresponding to the electron configuration 3d<sup>7.5</sup>. The implied multiplicity of the active 3d electrons is reminiscent of the Fe-based superconductors [10–12]. Ab initio calculations further suggest that the  $z^2$  and  $x^2 - y^2$  3d orbitals are important to the low-energy electronic structure [13]. Accordingly, there are N = 3 electrons per bilayer unit cell that are active in the manifold of Ni  $e_q$  orbitals. All these point towards the importance of orbital-selective correlations in  $La_3Ni_2O_7$ , as we have emphasized in Ref. [14]. Other theoretical approaches to the electron correlations have also been taken [15–20]. More generally, the origin of the high-temperature superconductivity in La<sub>3</sub>Ni<sub>2</sub>O<sub>7</sub> has been the focus of enormous theoretical efforts [21–56].

The effects of electron correlations in bilayer nickelates have been studied in experiments at ambient pressure. Four salient features have emerged. First, a recent mea-

surement of optical conductivity [57] reported a substantially suppressed Drude weight compared to the band theory value. Second, an ARPES experiment [58] found strong orbital-dependent band renormalizations, suggesting orbital-selective electron correlations in the system. While both points indicate substantial band renormalization effect, the spectroscopy measurements provide two further constraints on the theoretical description. As the third point, the interband peak of the optical spectra, located at about 1 eV, seems to exhibit relatively weak renormalization effect compared to the density functional theory (DFT) results [57, 59]. The fourth point concerns whether or not the  $z^2$  bonding band (the  $\gamma$  band) crosses the Fermi level  $(E_F)$ . This influences the Fermi surface topology and is possibly important to the superconductivity at high pressure. The aforementioned ARPES experiment revealed that this band is located about 50 meV below the Fermi level and its energy position is almost temperature independent, implying that this gap to  $E_F$ is unrelated to the density wave ordering. Qualitatively, a strong band renormalization effect could enable such a gap; however, it would seem that such an effect is incompatible with the weak renormalization of the observed interband optical conductivity peak. Taken together, these four points represent a challenge to a comprehensive theoretical description.

In this Letter, we provide a coherent understanding of all these points in a bilayer two-orbital Hubbard model for  $\text{La}_3\text{Ni}_2\text{O}_7$  in terms of orbital-selective electron correlations, which we characterize through a proposed global phase diagram of the Coulomb interaction strength (U) and electron density (N) as given in Fig. 1a. We show

that a Mott transition develops with increasing U when the electron density is taken to be at half filling (N=4); the resulting Mott insulator anchors the strong orbitalselective behavior of the system when N moves away from half filling up to the physical electron count N=3. In addition, the strong orbital selectivity causes an effective interlayer antiferromagnetic (AFM) exchange interaction between electrons in the  $z^2$  orbital. The AFM interaction further bounds the electrons between the top and bottom layers to an interlayer spin singlet and this causes an additional splitting between the bonding and antibonding  $z^2$  bands. By calculating the band structure and the optical conductivity in the model, we show that our theory provides the understanding of the strong orbital-selective band renormalization and the sinking of the  $\gamma$  band, along with the substantially reduced Drude weight and yet the weakly shifted interband peak in the optical conductivity.

Model and method. We consider a bilayer Hubbard model of two orbitals, corresponding to the 3d  $z^2$  and  $x^2 - y^2$  orbitals. The Hamiltonian reads as  $H = H_{\rm TB} + H_{\rm int}$ . The tight-binding Hamiltonian is as follows:

$$H_{\text{TB}} = \frac{1}{2} \sum_{i\delta ll'\alpha\beta\sigma} t_{\delta ll'}^{\alpha\beta} d_{il\alpha\sigma}^{\dagger} d_{i+\delta l'\beta\sigma} + \sum_{il\alpha\sigma} (\epsilon_{\alpha} - \mu) d_{il\alpha\sigma}^{\dagger} d_{il\alpha\sigma}$$

Here,  $d^{\dagger}_{il\alpha\sigma}$  creates an electron in orbital  $\alpha$  with spin  $\sigma$  at site i of the square lattice in layer l (with l=1,2 denoting the top and bottom layers, respectively),  $\epsilon_{\alpha}$  refers to the energy level associated with the crystal field splittings, and  $\mu$  is the chemical potential. The tight-binding parameters can be found in the Supplemental Materials (SM) [60]. In addition, the interacting Hamiltonian contains the dominant on-site interactions:

$$H_{\text{int}} = \frac{U}{2} \sum_{i,l,\alpha,\sigma} n_{il\alpha\sigma} n_{il\alpha\bar{\sigma}} + \sum_{i,l,\alpha<\beta,\sigma} \left\{ U' n_{il\alpha\sigma} n_{il\beta\bar{\sigma}} + (U' - J_{\text{H}}) n_{il\alpha\sigma} n_{il\beta\sigma} \right.$$

$$\left. - J_{\text{H}} (d^{\dagger}_{il\alpha\sigma} d_{il\alpha\bar{\sigma}} d^{\dagger}_{il\beta\bar{\sigma}} d_{il\beta\sigma} + d^{\dagger}_{il\alpha\sigma} d^{\dagger}_{il\alpha\bar{\sigma}} d_{il\beta\sigma} d_{il\beta\bar{\sigma}}) \right\},$$

$$\left. - J_{\text{H}} (d^{\dagger}_{il\alpha\sigma} d_{il\alpha\bar{\sigma}} d^{\dagger}_{il\alpha\bar{\sigma}} d_{il\beta\sigma} + d^{\dagger}_{il\alpha\sigma} d^{\dagger}_{il\alpha\bar{\sigma}} d_{il\beta\sigma} d_{il\beta\bar{\sigma}}) \right\},$$

where  $n_{il\alpha\sigma} = d^{\dagger}_{il\alpha\sigma}d_{il\alpha\sigma}$ . Here, U, U', and  $J_{\rm H}$ , respectively denote the intra- and inter- orbital repulsions and the Hund's rule coupling, with  $U' = U - 2J_{\rm H}$  taken [61].

We study the model by the U(1) slave-spin method as detailed in Refs. [62] and [63]. To capture the effects of the strong interlayer hopping in the  $z^2$  orbital, we perform the calculation in a two-site unit cell and rotate the atomic basis for this orbital to the bonding (+) and antibonding (-) one defined as  $d_{i\pm\sigma} = \frac{1}{\sqrt{2}}(d_{i1z\sigma} \pm d_{i2z\sigma})$ . Importantly, by going beyond the approximation of projecting out the antibonding  $z^2$  orbital [14], we will be able to connect the physics at the physical N=3 to what happens at nearby electron fillings, including the half filling

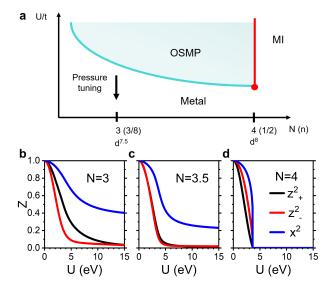


FIG. 1. a The proposed ground-state phase diagram with U and electron occupation number at nonzero Hund's coupling J<sub>H</sub> of the bilayer two-orbital Hubbard model for La<sub>3</sub>Ni<sub>2</sub>O<sub>7</sub>, anchored by the calculations shown in b-d and Fig. S3a of the SM [60]. The red line denotes a Mott insulator (MI) where both orbitals are localized. The shaded regime away from .half-filling stands for an orbital-selective Mott phase (OSMP) where electrons in the  $z^2$  orbital are localized while those in the  $x^2 - y^2$  orbital remain itinerant. The system exhibits (1)  $\frac{x-y}{\text{strong orbital-selective behavior even outside (though still in$ proximity of) the OSMP. Accordingly, the black arrow marks the parameter regime for La<sub>3</sub>Ni<sub>2</sub>O<sub>7</sub>. The electron filling factors and configurations are marked under the horizontal axis. **b-d** Evolution of the orbital-resolved quasiparticle spectral weight Z with U in the bilayer two-orbital Hubbard model for  $J_{\rm H}/U=0.25$  and at electron numbers  $N=3,\,N=3.5,$ and N=4, respectively, showing the strong orbital-selective bahavior and, for N=4, the Mott transition.

at N=4. The results thus obtained are verified to be robust based on calculations using the rotational invariant Gutzwiller variational method [64, 65].

Global phase diagram and strong orbital-selectivity. In Fig. 1b we show the evolution of the orbital-resolved quasiparticle spectral weight  $Z_{\alpha}$  with U for  $J_{\rm H}/U=0.25$  at electron number N=3 in the bilayer two-orbital Hubbard model, which corresponds to the physical electron count for the electron configuration  $d^{7.5}$  per Ni ion. For  $U\gtrsim 3$  eV the system exhibits strong orbital selectivity, with the electrons in the  $z^2$  orbitals being more correlated than those in the  $x^2-y^2$  orbital as the former have a narrower bare bandwidth (see Fig. S1 of SM [60]).

To understand the strong orbital selective behavior at N=3, we examine  $Z_{\alpha}$  with U for N=3.5 and N=4. As shown in Fig. 1c and d, both the quasiparticle weight renormalization and orbital selectivity are stronger with increasing N; for N=4 where the model is at half filling, a Mott transition develops with increasing U to about 4 eV. These results lead to the phase diagram sketeched in

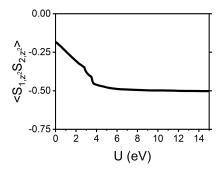


FIG. 2. Evolution of the interlayer spin correlator in the  $z^2$  orbital of the bilayer two-orbital model at N=3. The flatness of the curve suggests interlayer spin-singlet formation of the  $z^2$  orbital electrons.

Fig. 1a; additional results for further intermediate values of N are given in Fig. S3 of the SM [60]. The strong orbital-selective behavior away from half filling can then be naturally understood as doping a putative Mott insulator (MI) at half filling (N=4), an effect reminiscent of the strong correlations in heavily hole-doped iron pnictides [66, 67].

Formation of interlayer spin singlet. The behavior of  $Z_{\alpha}$  in Fig. 1b shows that the strong orbital selectivity exists in a broad regime of U values. In this regime, the two  $z^2$  orbitals are nearly localized, and are close to half filling (Fig. S3b of SM [60]). This clearly indicates development of quasi-localized magnetic moments. Given the large interlayer hopping  $t_z^{11}$  in the  $z^2$  orbital, we expect the two moments to interact via an antiferromagnetic (AFM) superexchange coupling and hence form an interlayer spin singlet. We calculate the interlayer (equal time) spin correlator  $\langle \mathbf{S}_{1,z^2} \cdot \mathbf{S}_{2,z^2} \rangle$  for electrons in the  $z^2$  orbital, and the result is shown in Fig. 2. The spin correlator decreases with increasing U monotonically and reaches a large negative value for  $U \gtrsim 4$  eV, where the system exhibits strong orbital selectivity. In this regime it almost saturates to about -0.5. The negative sign indicates the interaction between the moments are indeed AFM, and the almost saturation of the correlation function implies the formation of interlayer spin singlet. Note that the magnitude is still smaller than the value (-3/4)for a perfect spin singlet, which reflects the moments not being fully localized, as the  $z^2$  orbitals are not exactly at half filling.

The spin singlet state has a finite gap  $\Delta$  to the triplet excitation. This gap can be equated to  $J_{z^2-z^2}$ , the interlayer superexchange coupling in the  $z^2$  orbital channel. This allows us to estimate the effective superexchange coupling between these moments from the low-temperature behavior of  $\langle \mathbf{S}_{1,z^2} \cdot \mathbf{S}_{2,z^2} \rangle$ , which is detailed in the SM [60]. The extracted  $J_{z^2-z^2}$  values are shown in Fig. S4b of the SM [60]. The non-monotonic behavior of  $J_{z^2-z^2}$  with U indicates a clear crossover between weak and strong orbital-selective electron correla-

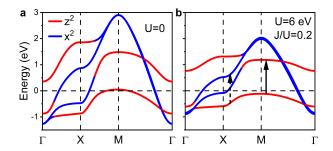


FIG. 3. Calculated band structures of the bilayer two-orbital Hubbard model for N=3 at U=0 (in a) and U=6 eV with  $J_{\rm H}/U=0.2$  (in b). The blue and red colors indicate the major orbital characters of the bands are  $x^2-y^2$  and  $z^2$ , respectively. The Fermi energy  $E_F=0$  is set. The dashed and solid arrows denote typical processes that contribute to  $\sigma_{xx}$  and  $\sigma_{zz}$ , respectively.

tions [68]. While  $J_{z^2-z^2}$  for realistic U values is smaller than the atomic-limit based estimation, it still is sizable.

Implications for spectroscopy. The strong orbital selectivity and the formation of spin singlet in the model have important effects on the band structure which can be detected by the ARPES spectra and will be manifested in the optical conductivity. In Fig. 3 we compare the band structures of the model at U=0 and U=6 for  $J_{\rm H}/U=0.2$  at N=3. The correlation effect is first seen as a substantial suppression of the overall bandwidth. Another prominent effect is that the flat bonding  $z^2$  band near the M point sinks to slightly below  $E_F$ . This removes the small hole pocket near the M point and only slightly changes the volumes of the other Fermi pockets.

To see the orbital-selective band renormalization behavior, we extract the effective mass enhancement factor  $m^*/m_0$  of bands near  $E_F$  along several cuts in the BZ that correspond to those studied in a recent ARPES experiment [58]. The cuts are shown in Fig. S2b, and the  $m^*/m_0$  values estimated from velocity ratios for U=6eV are summarized in Table I. The bands mainly have  $x^2 - y^2$  orbital characters along cuts 1 and 2, while they are dominated by the bonding  $(z_+^2)$  orbital along cuts 4 and 5. Accordingly, the orbital selectivity causes an orbital-dependent effective mass enhancement, as observed in the ARPES measurement. Along cut 3, the band has a mixed character between the  $x^2 - y^2$  and the  $z^2$  orbitals and  $m^*/m_0$  takes an intermediate value. In Table I, we also list the  $m^*/m_0$  values determined from the ARPES experiment [58]. Our results agree with the experimental ones semi-quantitatively.

One surprising feature in our calculation is that the splitting between the bonding and antibonding  $z^2$  bands remains to be large at about 1 eV although the bandwidths are substantially renormalized under strong correlations. This is clearly seen by comparing the bands at U=0 and U=6 eV in Fig. 3. This reflects the renormalization of the electronic energy dispersion by the sizable

TABLE I. Comparison between our theoretical results with the measurements of Ref. [58] on the effective mass enhancement factor  $m^*/m_0$  of bands near  $E_F$  along several cuts in the BZ shown in Fig. S2 of the SM [60].

	ARPES	$U = 6 \text{ eV}, J_{\rm H}/U = 0.25$
Cut 1	1.8	2.5
Cut 2	2.3	1.7
Cut 3	2.6	3.3
Cut 4	7.7	4.6
Cut 5	5.0	4.6

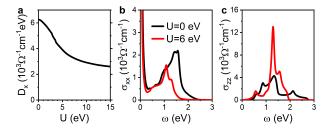


FIG. 4. **a** The evolution of Drude weight  $D_x$  of the in-plane optical conductivity with U. **b** The in-plane optical conductivity  $\sigma_{xx}$  at U=0 and U=6 eV and  $J_H/U=0.2$ . **c** The out-of-plane optical conductivity  $\sigma_{zz}$  at U=0 and U=6 eV. A sharp peak emerges at U=6 eV when the  $z_+^2$  bonding band sinks below  $E_F$ .

interlayer spin-exchange interaction  $J_{z^2-z^2}$ , as described in detail in the SM [60]. It can also push the bonding band to below  $E_F$ . This well explains the almost temperature independence of the energy position of the  $\gamma$  band observed in ARPES because  $J_{z^2-z^2}$  is much larger than room temperature. To further verify that the exchange interaction leads to band splitting, we perform calculation within a single-site approximation, where the superexchange interaction is not taken into account. As shown in Fig. S5a, the bonding-antibonding splitting is substantially suppressed in this approximation [60].

We now turn to the optical conductivity. The calculated Drude weight  $D_x$  of the in-plane component of the optical conductivity  $\sigma_{xx}$  is shown in Fig. 4a.  $D_x$  decreases with increasing U, in a way that follows the behavior of the quasiparticle spectral weight Z. We find  $D_x(U)/D_x(0)$  approximately equals to the orbital averaged Z value, and for  $U \sim 6$  eV,  $D_x(U)/D_x(0) \sim 2$ . This reduction of the Drude weight by a factor of 2 is sizable, and captures the essence of the experimental observation. Quantitatively, the ratio extracted from the optical conductivity measurement [57] is even larger (on the order of  $\sim 10$ ), which could suggest that the relevant interaction strength is even larger or the need for orbital-resolved Drude weight estimate based on light polarization.

Besides the Drude weight, we also calculate the interband contribution of the optical conductivity and the overall results for U=0 and U=6 eV with  $J_{\rm H}/U=0.2$  are shown in Fig. 4b. At U=0,  $\sigma_{xx}$  develops a broad peak at 1.3-1.5 eV. With strong band renormalization, we would expect the peak shifts drastically to low energy, as shown in Fig. S5b. However, as shown in Fig. 4b, the interband peak only slightly shifts to lower energy at about 1 eV for U=6 eV. The reason for this is revealing of the underlying physics. The peak is mainly caused by the transition indicated by the dashed arrow (between the bonding  $z^2$  band and the band with hybridized antibonding  $z^2$  and  $z^2-y^2$  orbitals) in Fig. 3b, and the enhanced bonding-antibonding splitting by the superexchange interaction of local moments keeps the transition energy to be still at about 1 eV. Our result is consistent with the optical conductivity experiment [57].

To directly probe the bonding-antibonding splitting, we propose to measure the out-of-plane component  $\sigma_{zz}$ , which is contributed from intraorbital transitions by the polarization set up. As illustrated by the solid arrow in Fig. 3b, when the bonding band sinks to below  $E_F$ , such an interband transition would generate a sharp peak at about 1 eV in  $\sigma_{zz}$ , as shown in Fig. 4c. However, if the bonding band crosses  $E_F$ , the transition associated with the portion above  $E_F$  will no longer contribute;  $\sigma_{zz}$  would be substantially suppressed with the peak position almost unchanged, as can be inferred from Fig. 4c. Therefore, measuring  $\sigma_{zz}$  in the high-pressure phase would allow not only the determination of the bonding-antibonding splitting energy but also the assessment about whether the bonding state crosses the Fermi level.

Discussion and conclusion. In a previous study on the correlation effects of the bilayer two-orbital Hubbard model for  $\text{La}_3\text{Ni}_2\text{O}_7$ , we further simplified the problem by projecting out the higher-energy antibonding  $z^2$  orbital. The calculation reported here is crucial, as it allows us to study the N=3 system from a broader perspective of varying N. We find the correlations in the antibonding  $z^2$  orbital to be stronger than its bonding counterpart at N=3 (see Fig. 1b). This is because, when this orbital is allowed to be active, its high energy nature demands a narrower bandwidth for the kinetic energy to be minimized. Nonetheless, we find robustly strong orbital selectivity, and we are able to understand this surprising result in the framework of our newly proposed global phase diagram (c.f. Fig. 1a).

A recent experiment [7] on the  $\text{La}_3\text{Ni}_2\text{O}_7$  thin film showed that  $\text{O}_3$  annealing can turn the insulating sample to metallic (and becomes superconducting under cooling), accompanied by a valence increase of the Ni ion. The trend of the resistivity and valence changes can be well understood within our proposed global phase diagram: The annealing effectively increases the doping level, pushing the system away from the parent MI to a metal with strong orbital-selective correlations.

An important implication of the global phase diagram is that it allows for constructing a multiorbital t-J model

to study superconductivity that is applicable for the orbital-selective correlation regime. We expect the d-wave pairing, favored by the in-plane exchange coupling between electrons in the  $x^2-y^2$  orbital, to be in competition with the extended-s pairing, driven by the interlayer exchange coupling between electrons in the  $z^2$  orbital. An indepth analysis is left for future research [69].

In summary, we have studied the orbital-dependent electron correlations in a bilayer two-orbital Hubbard model for La<sub>3</sub>Ni<sub>2</sub>O<sub>7</sub>. We find strong orbital selectivity away from half filling that is ultimately anchored by a Mott insulator at half filling, a result that is encoded in a global phase diagram we have proposed (Fig. 1a). At the physical electron count N = 3, we show that the strong orbital selectivity leads to the formation of interlayer singlets between electrons in the  $z^2$  orbitals. The latter contribute to the strong renormalization of the band structure, in particular an enhanced splitting between the bonding and antibonding  $z^2$  bands. Together, these effects explain all four key features observed in the ARPES and optical conductivity measurements that we outlined in the introduction. Given the importance of the electronic structure to superconductivity, our results provide a basis to understand not only the normal state but also the high temperature superconductivity of the bilayer nickelates. More generally, our work enriches the microscopic physics that is crucial to correlated superconductivity in general.

We thank W. Ding and H. Y. Hwang for useful discussions. This work has in part been supported by the National Science Foundation of China (Grants 12334008 and 12174441). Work at Rice was primarily supported by the U.S. Department of Energy, Office of Science, Basic Energy Sciences, under Award No. DE-SC0018197, and by the Robert A. Welch Foundation Grant No. C-1411. Q.S. acknowledges the hospitality of the Aspen Center for Physics, which is supported by NSF grant No. PHY-2210452.

- \* These authors contributed equally to this study.
- † rong.yu@ruc.edu.cn
- † qmsi@rice.edu
- [1] Hualei Sun, Mengwu Huo, Xunwu Hu, Jingyuan Li, Zengjia Liu, Yifeng Han, Lingyun Tang, Zhongquan Mao, Pengtao Yang, Bosen Wang, Jinguang Cheng, Dao-Xin Yao, Guang-Ming Zhang, Meng Wang, Nature 621, 493 (2023).
- [2] Zehao Dong, Mengwu Huo, Jie Li, Jingyuan Li, Pengcheng Li, Hualei Sun, Lin Gu, Yi Lu, Meng Wang, Yayu Wang, Zhen Chen, Nature 630, 847 (2024).
- [3] Haozhe Wang, Long Chen, Aya Rutherford, Haidong Zhou, Weiwei Xie, Inorganic Chemistry 63, 5020 (2024).
- [4] Yazhou Zhou, Jing Guo, Shu Cai, Hualei Sun, Pengyu Wang, Jinyu Zhao, Jinyu Han, Xintian Chen, Yongjin Chen, Qi Wu, Yang Ding, Tao Xiang, Ho-kwang Mao,

- Liling Sun, (2023), arXiv:2311.12361.
- [5] Yanan Zhang, Dajun Su, Yanen Huang, Zhaoyang Shan, Hualei Sun, Mengwu Huo, Kaixin Ye, Jiawen Zhang, Zihan Yang, Yongkang Xu, Yi Su, Rui Li, Michael Smidman, Meng Wang, Lin Jiao, Huiqiu Yuan, Nature Physics 20, 1269 (2024).
- [6] Ningning Wang, Gang Wang, Xiaoling Shen, Jun Hou, Jun Luo, Xiaoping Ma, Huaixin Yang, Lifen Shi, Jie Dou, Jie Feng, Jie Yang, Yunqing Shi, Zhian Ren, Hanming Ma, Pengtao Yang, Ziyi Liu, Yue Liu, Hua Zhang, Xiaoli Dong, Yuxin Wang, Kun Jiang, Jiangping Hu, Stuart Calder, Jiaqiang Yan, Jianping Sun, Bosen Wang, Rui Zhou, Yoshiya Uwatoko, Jinguang Cheng, (2024), arXiv:2407.05681.
- [7] Eun Kyo Ko, Yijun Yu, Yidi Liu, Lopa Bhatt, Jiarui Li, Vivek Thampy, Cheng-Tai Kuo, Bai Yang Wang, Yonghun Lee, Kyuho Lee, Jun-Sik Lee, Berit H. Goodge, David A. Muller, Harold Y. Hwang, Nature (2024).
- [8] Danfeng Li, Kyuho Lee, Bai Yang Wang, Motoki Osada, Samuel Crossley, Hye Ryoung Lee, Yi Cui, Yasuyuki Hikita, Harold Y. Hwang, Nature 572, 624 (2019).
- [9] Patrick A. Lee, Naoto Nagaosa, Xiao-Gang Wen, Reviews of Modern Physics 78, 17 (2006).
- [10] Qimiao Si, Rong Yu, Elihu Abrahams, Nature Reviews Materials 1, 16017 (2016).
- [11] Anna E. Bohmer, Jiun-Haw Chu, Samuel Lederer, Ming Yi, Nature Physics 18, 1412 (2022).
- [12] Qimiao Si, Nigel E. Hussey, Physics Today 76, 34 (2023).
- [13] Zhihui Luo, Xunwu Hu, Meng Wang, Wei Wu, Dao-Xin Yao, Physical Review Letters 131, 126001 (2023).
- [14] Zhiguang Liao, Lei Chen, Guijing Duan, Yiming Wang, Changle Liu, Rong Yu, Qimiao Si, Physical Review B 108, 214522 (2023).
- [15] D. A. Shilenko, I. V. Leonov, Physical Review B 108, 125105 (2023).
- [16] Frank Lechermann, Jannik Gondolf, Steffen Botzel, Ilya M. Eremin, Physical Review B 108, L201121 (2023).
- [17] Yingying Cao, Yi-feng Yang, Physical Review B 109, L081105 (2024).
- [18] Zhenfeng Ouyang, Jia-Ming Wang, Jing-Xuan Wang, Rong-Qiang He, Li Huang, Zhong-Yi Lu, Physical Review B 109, 115114 (2024).
- [19] Siheon Ryee, Niklas Witt, Tim O. Wehling, Physical Review Letters 133, 096002 (2024).
- [20] Yuxin Wang, Kun Jiang, Ziqiang Wang, Fu-Chun Zhang, Jiangping Hu, (2024), arXiv:2401.15097.
- [21] Xing-Zhou Qu, Dai-Wei Qu, Jialin Chen, Congjun Wu, Fan Yang, Wei Li, Gang Su, Physical Review Letters 132, 036502 (2024).
- [22] Griffin Heier, Kyungwha Park, Sergey Y. Savrasov, Physical Review B 109, 104508 (2024).
- [23] Jun Zhan, Yuhao Gu, Xianxin Wu, Jiangping Hu, (2024), arXiv:2404.03638.
- [24] Yi-Heng Tian, Yin Chen, Jia-Ming Wang, Rong-Qiang He, Zhong-Yi Lu, Physical Review B 109, 165154 (2024).
- [25] Zhiming Pan, Chen Lu, Fan Yang, Congjun Wu, (2023), arXiv:2309.06173.
- [26] Wei-Xuan Chang, Sibo Guo, Yi-Zhuang You, Zi-Xiang Li, (2023), arXiv:2311.09970.
- [27] Jiangfan Wang, Yi-feng Yang, (2024), arXiv:2408.09774.
- [28] Qiong Qin, Yi-feng Yang, Physical Review B 108, L140504 (2023).
- [29] Zhihui Luo, Biao Lv, Meng Wang, Wei Wu, Dao-Xin Yao, npj Quantum Materials 9, 61 (2024).

- [30] Kun Jiang, Ziqiang Wang, Fu-Chun Zhang, Chinese Physics Letters 41, 017402 (2024).
- [31] Junkang Huang, Z. D. Wang, Tao Zhou, Physical Review B 108, 174501 (2023).
- [32] Yi-feng Yang, Guang-Ming Zhang, Fu-Chun Zhang, Physical Review B 108, L201108 (2023).
- [33] Chen Lu, Zhiming Pan, Fan Yang, Congjun Wu, Physical Review Letters **132**, 146002 (2024).
- [34] Chen Lu, Zhiming Pan, Fan Yang, Congjun Wu, Physical Review B 110, 094509 (2024).
- [35] Jie-Ran Xue, Fa Wang, Chinese Physics Letters **41**, 057403 (2024).
- [36] Jialin Chen, Fan Yang, Wei Li, Physical Review B 110, L041111 (2024).
- [37] Tatsuya Kaneko, Hirofumi Sakakibara, Masayuki Ochi, Kazuhiko Kuroki, Physical Review B 109, 045154 (2024).
- [38] Masataka Kakoi, Tatsuya Kaneko, Hirofumi Sakakibara, Masayuki Ochi, Kazuhiko Kuroki, Physical Review B 109, L201124 (2024).
- [39] Runyu Ma, Tianxing Ma, Congjun Wu, (2024), arXiv:2408.02031.
- [40] Yi-feng Yang, (2024), arXiv:2408.14294.
- [41] Hirofumi Sakakibara, Naoya Kitamine, Masayuki Ochi, Kazuhiko Kuroki, Physical Review Letters 132, 106002 (2024).
- [42] Qing-Geng Yang, Da Wang, Qiang-Hua Wang, Physical Review B 108, L140505 (2023).
- [43] Ruoshi Jiang, Jinning Hou, Zhiyu Fan, Zi-Jian Lang, Wei Ku, Physical Review Letters 132, 126503 (2024).
- [44] Hongquan Liu, Chengliang Xia, Shengjie Zhou, Hanghui Chen, (2023), arXiv:2311.07316.
- [45] Xing-Zhou Qu, Dai-Wei Qu, Wei Li, Gang Su, (2023), arXiv:2311.12769.
- [46] Hui Yang, Hanbit Oh, Ya-Hui Zhang, (2024), arXiv:2408.01493.
- [47] Hui Yang, Hanbit Oh, Ya-Hui Zhang, (2023), arXiv:2309.15095.
- [48] Jia-Xin Zhang, Hao-Kai Zhang, Yi-Zhuang You, Zheng-Yu Weng, Physical Review Letters 133, 126501 (2024).
- [49] Da-Chuan Lu, Miao Li, Zhao-Yi Zeng, Wanda Hou, Juven Wang, Fan Yang, Yi-Zhuang You, (2023), arXiv:2308.11195.
- [50] Zhen Fan, Jian-Feng Zhang, Bo Zhan, Dingshun Lv, Xing-Yu Jiang, Bruce Normand, Tao Xiang, Physical Review B 110, 024514 (2024).
- [51] Yao-Yuan Zheng, Wei Wu, (2023), arXiv:2312.03605.
- [52] Henning Schlomer, Ulrich Schollwock, Fabian Grusdt, Annabelle Bohrdt, (2023), arXiv:2311.03349.
- [53] Steffen Botzel, Frank Lechermann, Jannik Gondolf, Ilya M. Eremin, (2024), arXiv:2401.16151.
- [54] Steffen Botzel, Frank Lechermann, Takasada Shibauchi, Ilya M. Eremin, (2024), arXiv:2411.01935.
- [55] Hanbit Oh, Boran Zhou, Ya-Hui Zhang, (2024), arXiv:2405.00092.
- [56] Hanbit Oh, Ya-Hui Zhang, Physical Review B 108, 174511 (2023).
- [57] Zhe Liu, Mengwu Huo, Jie Li, Qing Li, Yuecong Liu, Yaomin Dai, Xiaoxiang Zhou, Jiahao Hao, Yi Lu, Meng Wang, Hai-Hu Wen, Nature Communications 15, 7570 (2024).
- [58] Jiangang Yang, Hualei Sun, Xunwu Hu, Yuyang Xie, Taimin Miao, Hailan Luo, Hao Chen, Bo Liang, Wenpei Zhu, Gexing Qu, Cui-Qun Chen, Mengwu Huo, Yaobo Huang, Shenjin Zhang, Fengfeng Zhang, Feng Yang,

- Zhimin Wang, Qinjun Peng, Hanqing Mao, Guodong Liu, Zuyan Xu, Tian Qian, Dao-Xin Yao, Meng Wang, Lin Zhao, X. J. Zhou, Nature Communications **15**, 4373 (2024).
- [59] Benjamin Geisler, Laura Fanfarillo, James J. Hamlin, Gregory R. Stewart, Richard G. Hennig, P.J. Hirschfeld, npj Quantum Materials 9, 89 (2024).
- [60] See Supplemental Information [http://link...] for details of the tight-binding model and supplemental results on orbital-selective correlation effects, which include Refs. [68, 70, 71].
- [61] C. Castellani, C. R. Natoli, J. Ranninger, Physical Review B 18, 4945 (1978).
- [62] Rong Yu, Qimiao Si, Physical Review B 86, 085104 (2012).
- [63] Rong Yu, Qimiao Si, Physical Review B 96, 125110 (2017).
- [64] Nicola Lanata, Hugo U. R. Strand, Xi Dai, Bo Hellsing, Physical Review B 85, 035133 (2012).
- [65] Shiyu Peng, Hongming Weng, Xi Dai, Computer Physics Communications 276, 108348 (2022).
- [66] Rong Yu, Jian-Xin Zhu, Qimiao Si, Current Opinion in Solid State and Materials Science 17, 65 (2013).
- [67] Felix Eilers, Kai Grube, Diego A. Zocco, Thomas Wolf, Michael Merz, Peter Schweiss, Rolf Heid, Robert Eder, Rong Yu, Jian-Xin Zhu, Qimiao Si, Takasada Shibauchi, Hilbert v. Lohneysen, Physical Review Letters 116, 237003 (2016).
- [68] Wenxin Ding, Rong Yu, Qimiao Si, Elihu Abrahams, Physical Review B 100, 235113 (2019).
- [69] G. Duan et al., in preparation.
- [70] www.quantum-espresso.org.
- [71] wannier.org.

## SUPPLEMENTAL MATERIAL – Orbital-selective electron correlations in high- $T_c$ bilayer nickelates: from a global phase diagram to implications for spectroscopy

Zhiguang Liao, <sup>1,\*</sup> Yiming Wang, <sup>2,\*</sup> Lei Chen, <sup>2,3</sup> Guijing Duan, <sup>1</sup> Rong Yu, <sup>1,4,†</sup> and Qimiao Si<sup>2,‡</sup>

<sup>1</sup>Department of Physics and Beijing Key Laboratory of Opto-electronic Functional Materials & Micro-nano Devices,

Renmin University of China, Beijing 100872, China

<sup>2</sup>Department of Physics & Astronomy, Extreme Quantum Materials Alliance,

Smalley Curl Institute, Rice University, Houston, Texas 77005, USA

<sup>3</sup>Department of Physics and Astronomy, Stony Brook University, Stony Brook, NY 11794, USA

<sup>4</sup>Key Laboratory of Quantum State Construction and Manipulation (Ministry of Education),

Renmin University of China, Beijing, 100872, China

#### DETAILS OF THE TIGHT-BINDING MODEL

To obtain the tight-binding model, we first perform the density functional theory (DFT) calculations under the plane wave basis using projector augmented-wave potentials with the Perdew-Burke-Ernzerhof exchange-correlation functional as implemented in the Quantum Espresso (QE) code [70]. Based on the DFT results, the tight-binding models are constructed with Ni  $e_g$  orbitals using the maximally localized Wannier functions scheme as implemented in the WANNIER90 code [71]. The model contains hopping parameters up to the 2nd-nearest-neighbors and the tight-binding parameters are listed in Table S1.

The band structure of the tight-binding model is shown in Fig. 3a of the main text. It corresponds to the band structure in the high-pressure phase. The band structure in the low-temperature phase can be obtained by folding the bands to the Brillouin zone corresponding to a double-in-size primitive cell. In Fig. 3a we find the splitting between the bonding and antibonding  $z^2$  bands to be  $2|t_z^{11}|\approx 1.3$  eV. The bonding band crosses the Fermi level (at  $E_F=0$ ), causing a small hole pocket centered at M point in the Brillouin zone as shown in Fig. S2a. Besides this pocket, the Fermi surface also contains an electron pocket centered at  $\Gamma$  point and a large hole pocket, both of which are dominated by the  $x^2-y^2$  orbitals. The density of states projected on to the two  $e_g$  orbitals is shown in Fig. S1. Compared to the  $x^2-y^2$  orbital, the  $z^2$  orbital has a much narrower bandwidth. We then expect stronger correlation effects in this orbital, as shown in the main text.

#### SUPPLEMENTAL RESULTS ON ORBITAL-SELECTIVE ELECTRON CORRELATION EFFECTS

### Orbital selectivity and formation of interlayer $z^2$ spin singlet

We have shown in the main text that the system contains strong orbital-selective electron correlations at the the physical electron count N=3, and this is understood in terms of a proximity to an orbital-selective Mott phase, which in turn is near a Mott insulator at N=4. In Fig. S3a we present a quantitative global phase diagram, which

TABLE S1. Tight-binding parameters (in eV) of the bilayer two-orbital model in this work.  $\epsilon_{\alpha}$  denotes the onsite-energy of the  $\alpha$  orbital.  $\alpha=1, 2$  represent  $z^2$  and  $x^2-y^2$  ( $x^2$ ) orbitals, respectively.  $t_x$  and  $t_{xy}$  refer to the nearest-neighbor (n.n.) and next nearest-neighbor (n.n.n.) in-plane hoppings,  $t_z$  and  $t_{xz}$  refer to the n.n. and n.n.n. interlayer hoppings, respectively.  $\pm$  means the parameters are positive along the x direction and negative along the y direction.

	$\alpha = 1$	$\alpha = 2$		
$\epsilon_{lpha}$	10.5124	10.8716		
$rac{\epsilon_{lpha}}{t_{\mu}^{lphaeta}}$	$\mu = x$	$\mu = xy$	$\mu = z$	$\mu = xz$
$\alpha\beta = 11$	-0.1123	-0.0142	-0.6420	0.0257
$\alpha\beta = 22$	-0.4897	0.0686	0.0029	0.0006
$\alpha\beta = 12$	$\pm 0.2425$			<del>=</del> 0.0370

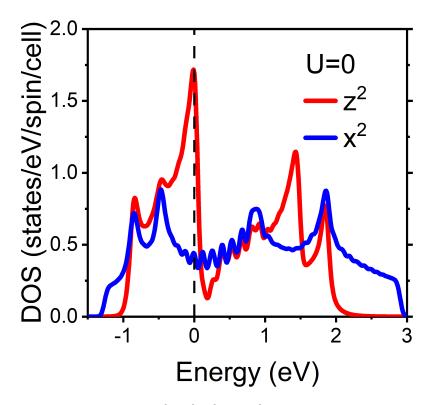


FIG. S1. Density of states (DoS) projected to the  $x^2 - y^2$  ( $x^2$ ) and  $z^2$  orbitals of the bilayer two-orbital tight-binding model (i.e., for U = 0 in the Hubbard model).

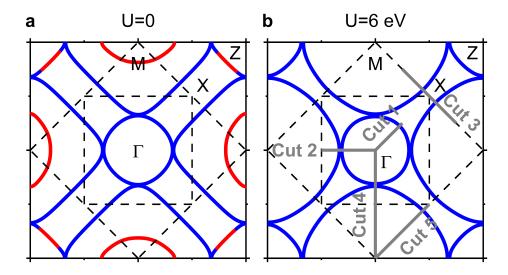


FIG. S2. Fermi surface of the bilayer two-orbital Hubbard model at U=0 (in **a**) and U=6 eV and  $J_{\rm H}/U=0.2$  (in **b**). The blue and red colors indicate that the dominant orbital characters are  $x^2-y^2$  and  $z^2$ , respectively. The minority orbital component, which is especially substantial near X in the Brillouin zone, is not marked.

extends the results shown in Fig. 1b-d of the main text. The phase diagram provides the basis for the schematic one shown in Fig. 1a, with a Mott transition at half filling (N=4), and an orbital-selective Mott phase (OSMP) away from half filling by doping the Mott insulator (MI). Importantly, the system already exhibits orbital-selective behavior, with the  $z^2$  orbital being more correlated, at a crossover  $U_{\rm cr}$  smaller than the onset of orbital-selective Mott or the Mott transition. This is a key to understanding the orbital-selective correlations in the N=3 case.

In Fig. S3b-d we also display the orbital-resolved electron fillings corresponding to N=3, N=3.5, and N=4.

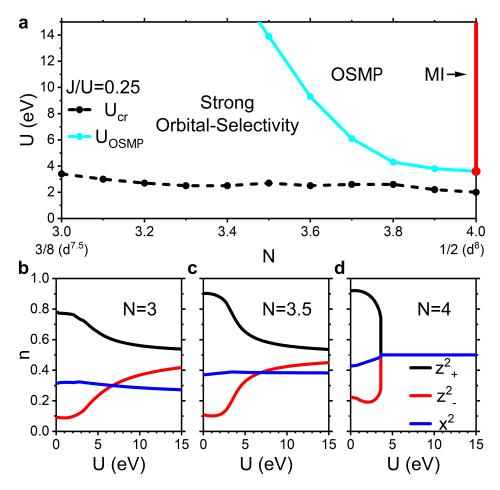


FIG. S3. a Ground-state phase diagram in the U-N plane of the bilayer two-orbital model for La<sub>3</sub>Ni<sub>2</sub>O<sub>7</sub> at  $J_{\rm H}/U=0.25$ . The system undergoes a Mott transition to a Mott insulator (MI) by increasing U at N=4, corresponding to half filling. The cyan line denotes the phase boundary of an orbital-selective Mott phase (OSMP) away from the half-filling. The dashed black line indicates a crossover to a strongly orbital-selective metallic phase by increasing U. We also mark the corresponding electron filling factors and configurations under the horizontal axis. **b-d** Evolution of the electron filling in each orbital with U for  $J_{\rm H}/U=0.25$  of the bilayer two-orbital model at N=3, N=3.5, and N=4, respectively.

Away from half-filling and at large U limit, the electrons in the  $z^2$  orbitals are closer to half-filling then in the  $x^2 - y^2$  orbitals. With the much stronger correlations in these orbitals, the results suggest that quasi-localized S = 1/2 moments develop in the  $z^2$  orbitals, as discussed in the main text. The claculated spin-spin correlation function in Fig. 2 of the main text implies that these quasi-local moments form interlayer spin singlets under antiferromagnetic (AFM) superexchange interaction. To extract the exchange coupling  $J_{z^2-z^2}$ , we calculate the spin-spin correlation function at low temperatures. When two moments form a spin singlet, it is gapped to the triplet excitations, and this causes the spin-spin correlation function to have an exponential behavior with the temperature, *i.e.*,

$$\langle \mathbf{S}_{1,z^2} \cdot \mathbf{S}_{2,z^2} \rangle \sim a + be^{-J_{z^2 - z^2}/T}.$$
 (S1)

Note that the excitation gap equals to the exchange coupling  $J_{z^2-z^2}$ , and considering that the moments are quasilocalized, we leave coefficients a and b in Eq. (S1) as free parameters. We fit the finite-temperature spin-spin correlation data with Eq. (S1), and a typical fitting result is shown in Fig. S4a. We can then extract the effective superexchange coupling  $J_{z^2-z^2}$ . The extracted values with U for  $J_{\rm H}/U=0.2$  is shown in Fig. S4b. In the large U limit,  $J_{z^2-z^2}$ increases with decreasing U and approximately follows the standard atomic limit behavior  $J \sim 4(t_z^{11})^2/U$  in a singleorbital model. In general, the Hund's coupling in a multiorbital model should give a correction to the J value in the single-orbital case [68]. Here we find  $J_{z^2-z^2}$  behaves similarly to J in the single-orbital limit because the  $x^2-y^2$  orbital is much less correlated and further away from half-filling compared to the  $z^2$  orbital.  $J_{z^2-z^2}$  develops a peak at  $U \sim 7$ eV and decreases rapidly with decreasing U. Together with the fast suppression of the magnitude of  $\langle \mathbf{S}_{1,z^2} \cdot \mathbf{S}_{2,z^2} \rangle$ ,

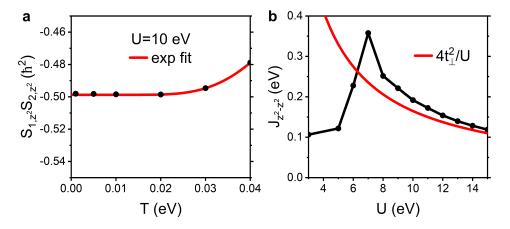


FIG. S4. **a** Finite-temperature spin-spin correlation function between electrons of the  $z^2$  orbital in the top and bottom layers. The red line is a fit using the exponential function in Eq. (S1). **b** Extracted AFM superexchange coupling  $J_{z^2-z^2}$  with U for  $J_{\rm H}/U=0.2$ . The red line shows a function  $4(t_z^{11})^2/U$ .

this leads us to the conclusion that well defined quasilocalized moments are not yet developed in the small U regime  $(U \lesssim 4 \text{ eV})$ . Note that the orbital selectivity is weak in this part of the phase diagram.

#### Additional bonding-antibonding splitting induced by the superexchange interaction

As shown in Fig. 3b, the splitting between the bonding and antibonding  $z^2$  bands is still sizable under strong electron correlations at U=6 eV. This is because the AFM superexchange interaction between quasi-localized moments in the  $z^2$  orbital can cause an additional splitting between the bonding and antibonding bands. To understand this, recall that the strong orbital selectivity in the system causes formation of the interlayer spin singlet. The Hamiltonian describing the interacting moments is

$$H_{SE} = J_{z^2 - z^2} \mathbf{S}_{1,z^2} \cdot \mathbf{S}_{2,z^2}. \tag{S2}$$

Given the electrons in the  $z^2$  orbital are not fully localized, this term affects the bandstructure. To see this, we rewrite  $H_{\rm SE}$  in the spin singlet channel

$$H_{\rm SE} = -\frac{J_{z^2-z^2}}{2} D_{12}^{\dagger} D_{12},$$
 (S3)

where  $D_{12} = \sum_{\sigma} d_{1\sigma}^{\dagger} d_{2\sigma}$  is the singlet operator in the  $z^2$  orbital. In the bonding-antibonding basis,  $D_{12} = n_+ - n_-$ , where  $n_{\pm} = \sum_{\sigma} d_{\pm\sigma}^{\dagger} d_{\pm\sigma}$ . After a saddle-point decomposition we get

$$H_{\rm SE} \approx -J_{z^2-z^2}(\langle n_+ \rangle - \langle n_- \rangle)(n_+ - n_-). \tag{S4}$$

Here,  $\langle n_+ \rangle - \langle n_- \rangle$  is precisely the difference of electron filling between the bonding and antibonding states. According to Eq. (S4), the interacting moments cause an additional splitting between the bonding and antibonding bands. For intermediate U values this splitting can be sizable as shown in Fig. 3b of the main text.

## Bandstructure and optical conductivity calculated from the single-site approximation

In this section, we show the results of bandstructure and optical conductivity within a single-site approximation and compare the results with those calculated based on the two-site unit cell and discussed in the main text. Note that within the singlet-site approximation, the interlayer correlation is only taken into account at a Hatree-Fock-like mean-field level so that the effective AFM interaction between quasi-local moments due to the singlet formation is not included. Therefore, the comparison between the single- and two-site calculations can clarify the effects of the interlayer spin singlet formation.

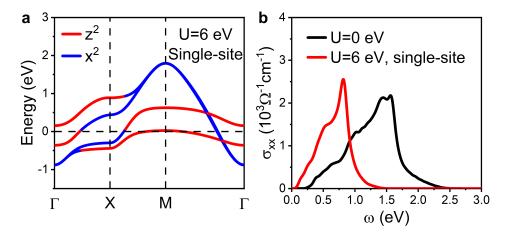


FIG. S5. a Bandstructures calculated at U=6 eV and  $J_{\rm H}/U=0.2$  within the single-site approximation (which does not consider any interlayer AFM superexchange interaction between the quasi-localized moments). **b** Optical conductivity within the single-site approximation at U=0 and U=6 eV with  $J_{\rm H}/U=0.2$ .

We first show the calculated bandstructure within the single-site approximation at U=6 eV and  $J_{\rm H}/U=0.2$  in Fig. S5a. Compared to the U=0 bandstructure in Fig. 3a of the main text, there is a prominent reduction of the overall bandwidth as a correlation effect. Because the interlayer hopping  $t_z^{11}$  is also renormalized and the splitting between the bonding and antibonding  $z^2$  bands is  $2t_z^{11}$ , the splitting between these two bands is substantially suppressed from about 1.3 eV to about 0.5 eV. This is to be contrast with the calculated result based on a two-site unit cell, where the separation between the two  $z^2$  bands remains to be about 1 eV, as shown in Fig. 3b of the main text. Such a big difference is because the AFM superexchange interaction between the quasi-local moments has an additional contribution to the bonding-antibonding splitting, as discussed in the main text and detailed in the previous subsection. This effect is captured within the two-site calculation but is not considered in the single-site one.

The effect of bonding-antibonding splitting in the bandstructure can be detected via optical conductivity. Without considering the AFM exchange interaction between quasi-local moments, the strong band renormalization shifts the interband peak of the optical conductivity from about 1.3-1.5 eV to about 0.7 eV, as shown in the single-site results in Fig. S5b. By contrast, in the two-site calculation, where the effects of AFM exchange interaction is considered, the interband peak is located at about 1 eV as shown in Fig. 4b of the main text, which is consistent with the experimental results.